

ARTICLE

Received 4 Aug 2014 | Accepted 19 May 2015 | Published 7 Jul 2015

DOI: 10.1038/ncomms8578

Engineering near-infrared single-photon emitters with optically active spins in ultrapure silicon carbide

F. Fuchs^{1,*}, B. Stender^{1,*}, M. Trupke², D. Simin¹, J. Pflaum^{1,3}, V. Dyakonov^{1,3} & G.V. Astakhov¹

Vacancy-related centres in silicon carbide are attracting growing attention because of their appealing optical and spin properties. These atomic-scale defects can be created using electron or neutron irradiation; however, their precise engineering has not been demonstrated yet. Here, silicon vacancies are generated in a nuclear reactor and their density is controlled over eight orders of magnitude within an accuracy down to a single vacancy level. An isolated silicon vacancy serves as a near-infrared photostable single-photon emitter, operating even at room temperature. The vacancy spins can be manipulated using an optically detected magnetic resonance technique, and we determine the transition rates and absorption cross-section, describing the intensity-dependent photophysics of these emitters. The on-demand engineering of optically active spins in technologically friendly materials is a crucial step toward implementation of both maser amplifiers, requiring high-density spin ensembles, and qubits based on single spins.

¹Experimental Physics VI, Julius-Maximilian University of Würzburg, Würzburg 97074, Germany. ²Vienna Center for Quantum Science and Technology, Atominstitut, TU Wien, Wien 1020, Austria. ³Bavarian Center for Applied Energy Research (ZAE Bayern), Würzburg 97074, Germany. *These authors contributed equally to this work. Correspondence and requests for materials should be addressed to V.D. (email: dyakonov@physik.uni-wuerzburg.de) or to G.V.A. (email: astakhov@physik.uni-wuerzburg.de).

Quantum emitters hosted in crystalline lattices are highly attractive candidates for quantum information processing¹, secure networks^{2,3} and nanosensing^{4,5}. For many of these applications it is necessary to have control over single emitters with long spin coherence times. Such single quantum systems have been realized using quantum dots⁶, colour centres in diamond⁷, dopants in nanostructures⁸ and molecules⁹. More recently, ensemble emitters with spin dephasing times in the order of microseconds and room-temperature optically detectable magnetic resonance (ODMR) have been identified in silicon carbide (SiC)^{10–12}, a compound being highly compatible to up-to-date semiconductor device technology. Until recently, however, the engineering of such spin centres in SiC on the single-emitter level has remained elusive¹³.

Silicon vacancy (V_{Si})-related defects in SiC have some advantages compared with other solid-state single-photon emitters. In particular, the zero-phonon lines (ZPLs) of V_{Si} -related defects in 4H and 6H polytypes of SiC present spectrally narrow features at near-infrared (NIR) wavelengths ($\lambda_{\text{ZPL}} = 850\text{--}1,200\text{ nm}$)^{10,14–16}. Rayleigh scattering losses in photonic structures are inversely proportional to the fourth power of the wavelength^{17,18}, giving almost one order of magnitude lower losses for these defects compared with the nitrogen-vacancy defect in diamond ($\lambda_{\text{ZPL}} = 637\text{ nm}$)¹⁹ or the carbon antisite-vacancy pair in SiC ($\lambda_{\text{ZPL}} = 660\text{ nm}$)²⁰. Similarly, scattering losses at interfaces and signal attenuation in optical fibers decrease with wavelength as well. Furthermore, V_{Si} -related defects in SiC can be integrated with existing optoelectronic devices²¹ and, in contrast to GaAs-based quantum dots²², operate even at room temperature.

Here, we demonstrate the control of spin centre density in ultrapure SiC over eight orders of magnitude, from below 10^9 to above 10^{16} cm^{-3} using neutron irradiation. For a low irradiation fluence, a fully photostable, room temperature, NIR single-photon emitter can clearly be isolated, demonstrating no bleaching even after 10^{14} excitation cycles. Based on their spectroscopic fingerprints, these centres are identified as silicon vacancies, which can potentially be used as qubits¹⁶, spin sensors²³ and maser amplifiers¹².

Results

Confocal microscopy. The 4H-SiC unit cell with a single V_{Si} defect is shown in Fig. 1a. The dangling bonds of four C atoms with the absent Si atom result in formation of energy levels within the forbidden gap (3.23 eV) of 4H-SiC^{24,25}. In case of negatively charged V_{Si} , five electrons form a spin quadruplet ($S = 3/2$) in the ground state^{12,26}. To excite these defects we use sub-band gap excitation of SiC at a laser wavelength of 785 nm ($h\nu = 1.58\text{ eV}$), which is close to their optimal excitation wavelength²⁷. At room temperature, the V_{Si} defects emit in the NIR spectral range from 800 to 1,100 nm. At cryogenic temperatures, two distinct ZPLs at $\lambda_{\text{ZPL}} = 862\text{ nm}$ (V1) and $\lambda_{\text{ZPL}} = 917\text{ nm}$ (V2), associated with two different crystallographic sites in 4H-SiC, are observed in the photoluminescence (PL) spectrum²⁸, which can be used as spectroscopic fingerprints of V_{Si} .

To control the V_{Si} density in a high-quality 110 μm thick 4H-SiC epitaxial layer²⁷, we used neutron irradiation ($0.18\text{ MeV} < E_n < 2.5\text{ MeV}$) in a fission reactor. The irradiation fluence was varied over more than eight orders of magnitude, from 10^9 to $5 \times 10^{17}\text{ cm}^{-2}$ (Fig. 1). Some parts of the generated V_{Si} defects are negatively charged because of the presence of residual N donors ($5.0 \times 10^{14}\text{ cm}^{-3}$). Additionally, the neutron transmutation doping may play a role^{29,30}. Such an unusual doping mechanism is caused by a nuclear reaction $^{30}\text{Si}(n,\gamma)^{31}\text{Si} \rightarrow ^{31}\text{P} + \beta^-$, when the capture of a neutron by the nuclear isotope ^{30}Si (natural abundance 3.2%) leads to the formation of an unstable isotope ^{31}Si . Followed by beta decay, it is converted into the stable isotope ^{31}P , resulting in additional n-type doping of SiC.

A PL confocal raster scan ($10 \times 10\text{ }\mu\text{m}^2$) on a sample irradiated with a low fluence of $n = 1 \times 10^{11}\text{ cm}^{-2}$ is presented in Fig. 1b. The PL is detected in the spectral range from 875 nm (owing to a longpass (LP) filter) to 1,050 nm (limited by the sensitivity of Si avalanche photodiodes (APDs)). Four, nearly diffraction-limited spots (full-width at half-maximum of $\sim 500\text{ nm}$) are clearly seen in this scan. With rising irradiation fluence to $n = 1 \times 10^{14}\text{ cm}^{-2}$ the number of PL spots increases as well (Fig. 1c). For the highest irradiation fluence of $n = 5 \times 10^{17}\text{ cm}^{-2}$, single PL spots cannot be resolved anymore and the PL spatial distribution becomes highly homogeneous (Fig. 1d). Remarkably, in the negligibly weak

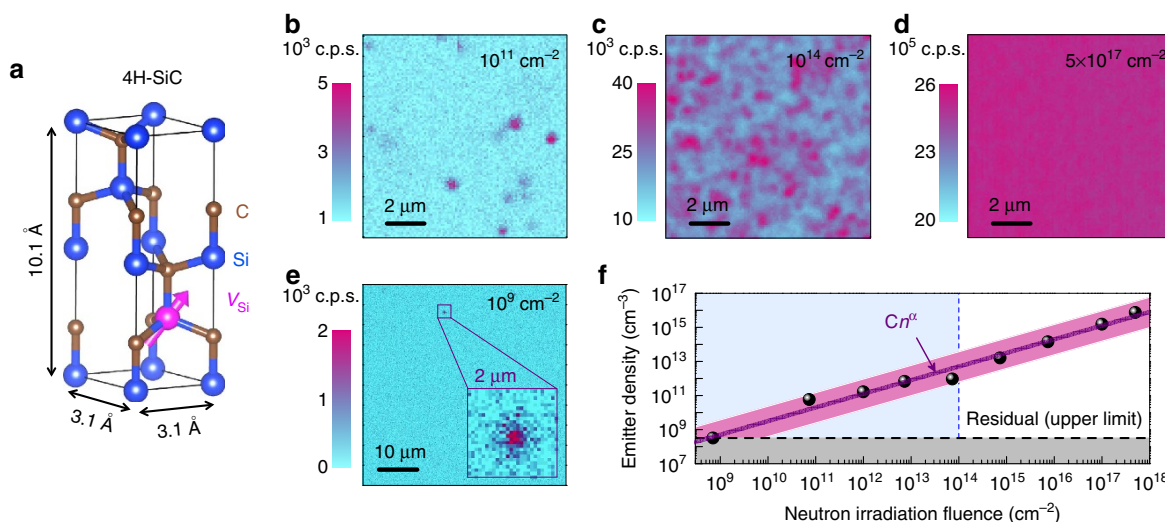


Figure 1 | Generation of V_{Si} defects in ultrapure 4H-SiC samples by neutron irradiation. (a) A scheme of the 4H-SiC unit cell with a single V_{Si} defect. (b–d) Confocal microscopy raster scans ($10 \times 10\text{ }\mu\text{m}^2$) for different neutron irradiation fluences: (b) $n = 1 \times 10^{11}\text{ cm}^{-2}$, (c) $n = 1 \times 10^{14}\text{ cm}^{-2}$ and (d) $n = 5 \times 10^{17}\text{ cm}^{-2}$. (e) A confocal microscopy raster scan ($50 \times 50\text{ }\mu\text{m}^2$) with a single V_{Si} defect (shown in the inset) for $n = 1 \times 10^9\text{ cm}^{-2}$. (f) Concentration of single-photon emitters \mathcal{N} as a function of the irradiation fluence. For low irradiation fluences up to the vertical dashed line, the concentration is found by direct count of emitters in the given volume. The solid line is a fit to $\mathcal{N} = Cn^\alpha$ with $\alpha = 0.8$.

irradiated sample (fluence of $1 \times 10^9 \text{ cm}^{-2}$) only one PL spot is found in the $50 \times 50 \mu\text{m}^2$ raster scan (Fig. 1e). The single spots are also restricted along the optical axis as shown in Fig. 2a. Below we unambiguously prove that these intensity spots are due to the emission from single V_{Si} defects.

Defect density. In order to find the density of single V_{Si} photon emitters the following procedure is used. Up to the irradiation fluence of $n = 1 \times 10^{14} \text{ cm}^{-2}$ we directly count the number of PL spots in the detection volume, given by the scanned area and the focus depth, the latter is about $1.2 \mu\text{m}$ according to Fig. 2a. For this irradiation fluence we also measure the integrated PL intensity collected from an area of $\sim 100 \mu\text{m}^2$. This PL is used as a reference to calculate the emitter density in the strongly irradiated samples by comparing their PL intensities. The results are presented in Fig. 1f. For the lowest irradiation fluence the defect density is $\mathcal{N} = 3 \times 10^8 \text{ cm}^{-3}$, which can be taken as the upper limit of residual V_{Si} concentration in our 4H-SiC sample. The concentration after the highest irradiation fluence constitutes $\mathcal{N} = 7 \times 10^{15} \text{ cm}^{-3}$. The real value can be even higher due to the generation of other types of defects with nonradiative recombination channels leading to a reduction of the PL intensity.

The irradiation fluence dependence follows quite well a power law \mathcal{N}^α with $\alpha = 0.8 \pm 0.1$, as shown by the solid line in Fig. 1f. This empirical power law can be used for the calculation of the required irradiation fluence to create silicon vacancy of desired concentration. Theoretical modeling of the defect creation process is beyond the scope of this paper. Qualitatively, the sublinear dependence can be explained by the creation of some other types of defects at the silicon sites of the SiC lattice, such

that at these sites a silicon vacancy cannot be created. However, this effect is relatively weak as α is close to one.

To identify the type of generated defects, we measure the PL spectra for different irradiation fluences. The spectrum from a single centre is identical to the ensemble emission (Fig. 2b). Here we use a LP filter 850 nm to suppress the excitation light at 785 nm in the detection path. The LO phonon Raman line of 4H-SiC at 850 nm is independent of the irradiation fluence and hence is masked by the stronger PL band for $n = 10^{15} \text{ cm}^{-2}$. We therefore use an additional LP filter 875 nm when investigating single centres. The PL spectra recorded at low temperature ($T = 5 \text{ K}$) are presented in Fig. 2c. Two characteristic lines at 861.4 and 916.3 nm are clearly visible for different irradiation fluences. These lines coincide with the V1 and V2 ZPLs²⁸, proving that the PL originates from the V_{Si} defects in 4H-SiC. These lines have different intensity, which may be due to their different polarization¹⁴ as in our experiments we are sensitive to the dipoles, which are polarized perpendicular to the c axis of SiC.

Single defect characterization. As expected for single defect centres, the PL intensity I saturates with increasing excitation power density W (Fig. 2d). After subtracting the linear background contribution and APD dark counts, it follows:

$$I(W) = \frac{I_{\max}}{1 + W_0/W}. \quad (1)$$

Here, $W_0 = 52 \text{ kW cm}^{-2}$ is the saturation power density exposed to the sample, corresponding to the laser power $P_0 = 0.3 \text{ mW}$ at the objective entrance aperture. The saturation PL intensity varies slightly from spot to spot and in Fig. 2d yields $I_{\max} = 8.5 \times 10^3$ counts per second (c.p.s.).

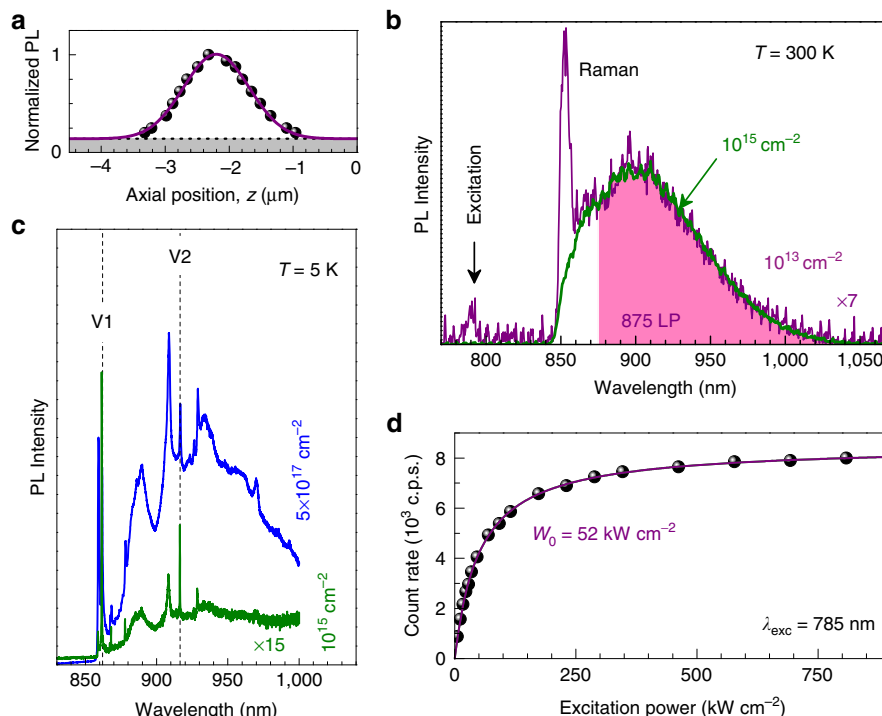


Figure 2 | NIR emission of a single V_{Si} defect in 4H-SiC. (a) PL line scan through a single V_{Si} defect. The top of the undoped 4H-SiC layer is placed at $Z = 0 \mu\text{m}$. Integrated PL is obtained with a LP filter at 875 nm. The solid line is a Gauss fit with a full-width at half-maximum of $1.2 \mu\text{m}$. (b) Room temperature PL spectrum of a single V_{Si} defect ($n = 10^{13} \text{ cm}^{-2}$) in comparison to a V_{Si} ensemble ($n = 10^{15} \text{ cm}^{-2}$). An 850 nm LP filter is used to suppress the excitation at 785 nm. An additional LP filter at 875 nm can be used to suppress a Raman line (LO phonon). (c) Low-temperature PL spectra of V_{Si} defects for different irradiation fluences. Two ZPLs, labeled as V1 and V2 (vertical dashed lines), are characteristic for two types of the V_{Si} defect in 4H-SiC. (d) Photon count rate of a single V_{Si} defect as a function of excitation power density. The solid line is a fit to Equation (1) with $W_0 = 52 \text{ kW cm}^{-2}$.

As a next step, we perform the Hanbury Brown and Twiss interferometry experiment, that is, the time correlation measurement of photon detection by two APDs. This is a frequently used method to verify single-photon emission^{19,20}. The second-order correlation functions $g^{(2)}(\tau)$, recorded over several hours for different W , are shown in Fig. 3b (see also Supplementary Note 2). The most important feature is the dip at zero time delay ($\tau = 0$). For the lowest excitation, we obtain $g^{(2)}(0) = 0.23 \pm 0.07 < 0.5$, which denotes clearly the nonclassical behavior of a single-photon emitter. In addition to the antibunching for $|\tau| < 15$ ns, there is also bunching for $|\tau| > 15$ ns. To explain such a behavior at least three levels have to be involved (Fig. 3a).

The second-order correlation function can be well described using

$$g^{(2)}(\tau) = 1 - (1 + a)e^{-|\tau|/\tau_1} + ae^{-|\tau|/\tau_2}, \quad (2)$$

as shown by the solid lines in Fig. 3b. The power dependencies of parameters a , τ_2 and τ_1 are presented in Fig. 3c–e, respectively. We use the same three-level model as for the colour centres in diamond^{19,31,32} to fit these dependencies. This model describes reasonably well the bunching amplitude $a(W)$ (the dashed line in Fig. 3c) and the antibunching decay time $\tau_1(W)$ (the dashed line in Fig. 3e). The transition rates obtained using these fits are summarized in Table 1. However, the relatively long bunching decay time $\tau_2(W)$ for $W < 100$ kW cm⁻² is not well reproduced at low excitation powers within this model (the dashed line in

Fig. 3d). A possible explanation is that a deshielding process of the metastable state $|3\rangle$ may occur under optical excitation³².

To describe the experimental data of Fig. 3 we consider a four-level model, where optical excitation from the metastable state to a higher-lying state and subsequent relaxation to the ground state occur (Fig. 3a). This results in intensity-dependent rate k_{31} , saturating for high W following³²

$$k_{31} = \frac{k_{31}^\infty - k_{31}^0}{1 + W_S/W} + k_{31}^0. \quad (3)$$

We use the procedure described in the Methods section to find all the transition rates k_{ij} and the results are summarized in Table 1. Using this approach we achieve a very good agreement with our experimental data (the solid lines in Fig. 3c–e). Remarkably, the excited state lifetime $(k_{21} + k_{23})^{-1} = 5.3$ ns agrees well with the PL decay time of 6.1 ns observed in time-resolved experiments²⁷ and is significantly longer than that of the band-to-band transition in semiconductor nanostructures³³.

Table 1 | Transition rates k_{ij} and absorption cross-section σ governing the population dynamics of V_{Si} .

Model	$1/k_{21}$	$1/k_{23}$	$1/k_{31}^0$	$1/k_{31}^\infty$	σ
3 Levels	7.6 ns	16.8 ns	—	107 ns	1.5×10^{-16} cm ²
4 Levels	7.8 ns	16.4 ns	150 ns	123 ns	1.1×10^{-16} cm ²

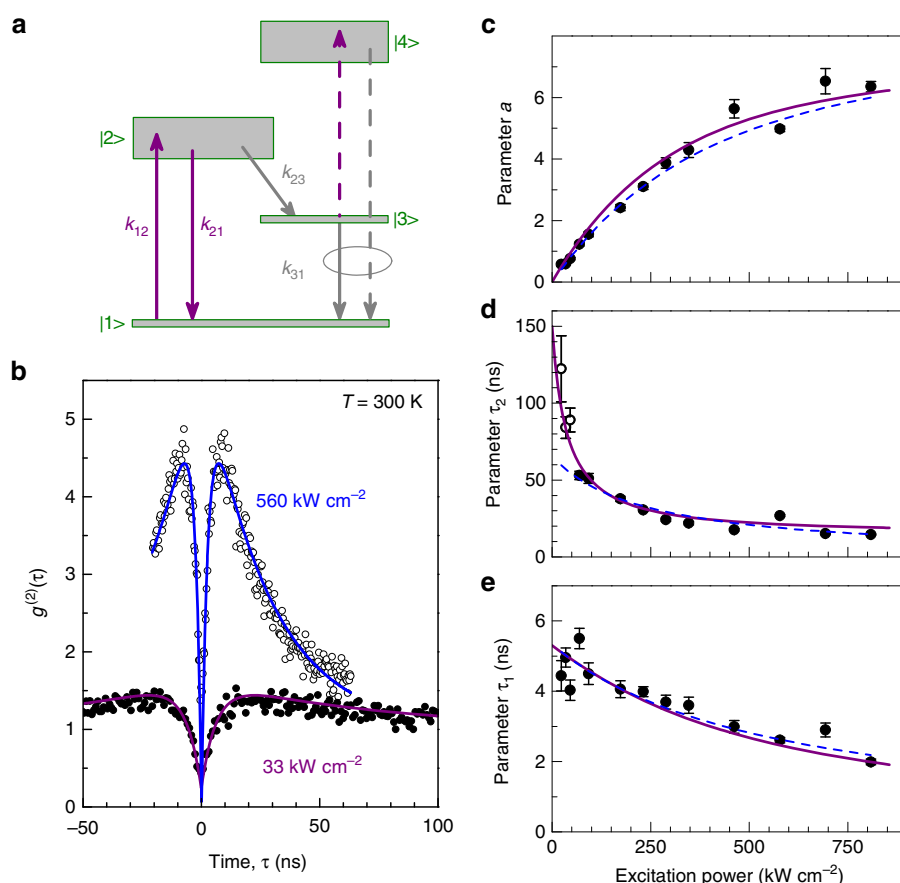


Figure 3 | Intensity correlation measurements at room temperature. (a) A four-level model of the V_{Si} defect with radiative recombination from the excited state $|2\rangle$ to the ground state $|1\rangle$ and nonradiative relaxation through the metastable state $|3\rangle$, which in turn can be optically activated to another excited state $|4\rangle$. (b) Correlation functions $g^{(2)}(\tau)$ recorded at two different excitation power densities $W < W_0$ and $W \gg W_0$. The solid lines are fits to Equations (2) (c–e) Fit parameters a , τ_1 and τ_2 of the antibunching curve as a function of excitation power density. The dashed and solid lines are fits to three-level and four-level model respectively, as discussed in the text.

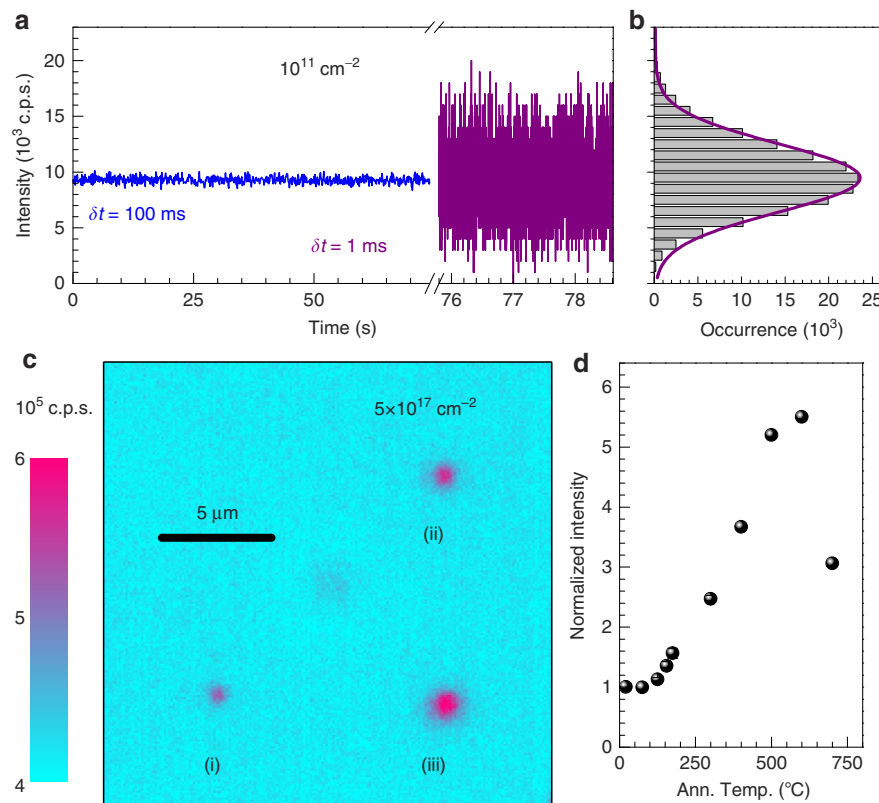


Figure 4 | Photostability of V_{Si} defects. (a) PL time traces with sampling bins $\delta t = 100 \text{ ms}$ and $\delta t = 1 \text{ ms}$, obtained on a single V_{Si} defect under excitation power density of $1,400 \text{ kW cm}^{-2}$. (b) Corresponding count rate histogram for $\delta t = 1 \text{ ms}$. The solid line is a Gauss fit. (c) A confocal microscopy raster scan ($20 \times 20 \mu\text{m}^2$) recorded after laser illumination of different spots for 120 min: spot (i) $P = 0.5 \text{ mW}$; spot (ii) $P = 1.5 \text{ mW}$; and spot (iii) $P = 3.5 \text{ mW}$. (d) Relative change of the V_{Si} PL intensity as a function of annealing temperature. The V_{Si} density before annealing is $\mathcal{N} = 7 \times 10^{15} \text{ cm}^{-3}$.

Photostability is an important characteristic of a single-photon emitter. The PL time trace of a single V_{Si} defect are shown in Fig. 4a. For a sampling bin to $\delta t = 100 \text{ ms}$, the count rate remains constant over minutes. To examine the photostability on a shorter time scale, the sampling bin is reduced to $\delta t = 1 \text{ ms}$. The number of detected photons per sampling bin is 10 in this case, and the time trace demonstrates statistical fluctuations without any indication of blinking (Fig. 4b). It should be indicated that blinking on much shorter time scales, if occurs, would not be detected in this case. We have also investigated a single V_{Si} emitter over more than 1 week under continuous excitation and did not observe photobleaching. Assuming that the excitation occurs on average every 10 ns, this corresponds to 10^{14} excitation cycles.

The maximum count rate of a single V_{Si} emitter in Fig. 4a is about 10^4 c.p.s. Using an optimized detection scheme with high detection efficiency of single photons as in the visible spectral range and with high optical transmission (above 90%) in the NIR, the count rate of about $4 \times 10^4 \text{ c.p.s.}$ should be achievable. However, this count rate is still lower as expected from the transition rates of Table 1. This discrepancy can partially be explained by a relatively high refractive index of SiC ($n_r = 2.6$), resulting in a large fraction of photons being restricted within the crystal due to the total internal reflection. To overcome this problem, one can either fabricate a solid immersion lens or use nanocrystals. In this case, together with optimized detection scheme a count rate above 10^5 c.p.s. is feasible.

Laser annealing. Finally we found that in the highly irradiated sample the PL intensity increases locally upon laser illumination.

To demonstrate this effect, the laser light of different intensities was focused sequentially on three different spots and remained there for 120 min, respectively. A confocal raster scan, performed at low laser power after such a procedure, demonstrates clearly a PL enhancement for each spot, as shown in Fig. 4c. For the highest laser power (spot (iii) in Fig. 4c) this enhancement is $\sim 25\%$. There are two possible mechanisms of this effect. One of them is that the laser changes the charge state of the defects. Remarkably, the generated pattern of Fig. 4c remains over many hours, indicating that discharging in the dark should also occur on the same time scale. Alternatively, the focused laser beam can locally heat up the sample, resulting in atomic displacements and thus in disappearance or/and transformation of some other types of intrinsic defects (for instance, recombination of Frenkel pairs or migration of interstitials)³⁴, generated upon neutron irradiation. These defects may serve as nonradiative recombination channels or as charge traps, switching off the V_{Si} defects in close proximity.

To show that heating indeed results in PL enhancement, we perform complementary annealing experiments by increasing stepwise the temperature and monitoring the integral PL intensity after each step. We prove that the PL spectrum remains unchanged (Supplementary Fig. 2). The results are summarized in Fig. 4d, showing the overall PL enhancement by a factor of 5.5. This corresponds to $\mathcal{N} = 3.9 \times 10^{16} \text{ cm}^{-3}$ and demonstrates that V_{Si} defects can be created at high density in a controlled manner, as required, for instance, for the implementation of a SiC maser¹².

Discussion

As has been mentioned in the introductory part, the generation of optically active spins is important for solid-state quantum

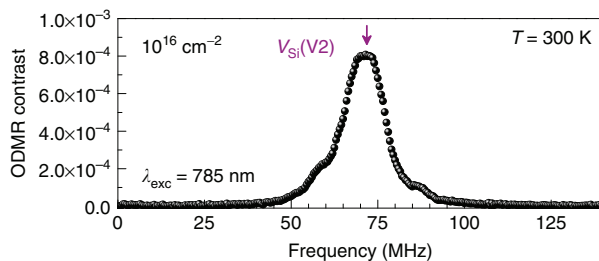


Figure 5 | Room-temperature ODMR spectrum of $\sim 10^4$ V_{Si} defects. The side peaks are due to uncompensated weak magnetic fields.

computing and communications, sensing, precision measurement and so on^{1–5,12,16,23}. Very recently, single emitters in the visible spectral range have been isolated in SiC wafers²⁰ and nanoparticles³⁵. However, these emitters do not reveal such spin properties. To demonstrate that the V_{Si} emitters engineered in the present work possess optically active spins, we perform ODMR experiments at room temperature (Fig. 5). The ODMR maximum is observed at 71 MHz, corresponding well to the zero-field spin splitting of $V_{\text{Si}}(\text{V}2)$ in 4H-SiC in much dense V_{Si} ensemble²³. The experiment of Fig. 5 has been performed on the sample with irradiation fluence of 10^{16}cm^{-2} , corresponding to $\sim 10^4$ simultaneously detected V_{Si} spins, as follows from Fig. 1f. This approach can be used to probe single spins as well, but with correspondingly increased readout time.

In our experiments, we precisely control the concentration of V_{Si} defects in ultrapure 4H-SiC down to single defect level. This approach can be used to deterministically incorporate³⁶ these atomic-scale defects in electronic²¹ and photonic structures³⁷ as well as in nanocrystals³⁸. Together with their extremely narrow optical resonances (on the order of 0.01 nm at low temperature¹⁶) and recently demonstrated optically detected spin resonances at ambient conditions²³, our results open exciting opportunities for various quantum applications with spin-photon interface.

Note, when the manuscript was in the reviewing process, we learnt about two papers where the coherent control of single spins in SiC is reported^{39,40}. Using a solid immersion lens, a count rate of 4×10^4 c.p.s. has been achieved⁴⁰, supporting the conclusions drawn here.

Methods

Samples. The 4H-SiC sample has been purchased from CREE. A high purity (residual nitrogen doping below $5.0 \times 10^{14}\text{cm}^{-3}$) layer of $110\mu\text{m}$ thickness was epitaxially grown on a 2-inch n-type 4H-SiC wafer. The layer is covered by a $5\mu\text{m}$ thick n-type 4H-SiC layer and a $2\mu\text{m}$ thick p-type 4H-SiC layer. The wafer was diced in $4\text{mm} \times 2\text{mm}$ pieces, which were then irradiated in a TRIGA Mark-II nuclear reactor, with neutron energies in the range of $0.18\text{MeV} < E_n < 2.5\text{MeV}$ (see also Supplementary Note 1). Further information on the reactor is available at <http://ati.tuwien.ac.at/reactor/EN/>.

The sample with the highest neutron irradiation fluence of $5 \times 10^{17}\text{cm}^{-2}$ was thermally annealed in several steps from 125 to 700°C for a time of 90 min, respectively. The heating was either performed on a heat stage ($125\text{--}200^\circ\text{C}$) or in an oven ($300\text{--}700^\circ\text{C}$).

Experimental setup. Samples were investigated with a home-build confocal microscope (Supplementary Fig. 1) and a cw 785 nm laser was used for excitation. A three-dimensional piezo unit (nPoint) was used to move the SiC sample in lateral and axial directions. The excitation beam was focused onto the samples by a high aperture ($\text{NA} = 1.49$) oil immersion microscope objective (UAPON 100XOTIRF, Olympus) with optical transmission in the NIR of about 60%. Collimated optical response of the sample was collected by the same objective and guided through a 30 or $75\mu\text{m}$ pinhole (Thorlabs) followed by a 850 and 875 nm LP filter (Edmund Optics). Time correlated single-photon counting (TCSPC) was recorded by a Hanbury Brown and Twiss setup consisting of two APDs (Count-100C-FC, Laser-components GmbH) with a quantum efficiency of ~ 0.3 at the signal wavelength and < 100 c.p.s. in the dark and a 16-channel photon correlator card (DPC-230, Becker & Hickl GmbH) with a time resolution of at least 165 ps.

The low-temperature PL spectra were measured at 5 K in a cryostat (MicrostatHe, Oxford Instruments) built into a confocal Raman spectrometer (LabRAM HR, Horiba). The excitation wavelength was 633 nm. In the ODMR experiment, the radio frequency radiation provided by a signal generator is amplified and guided to a thin copper wire terminated with a 50 Ohm impedance. We use a standard lock-in detection scheme, described elsewhere²³.

Fitting procedure. In order to find the transition rates k_{ij} of the four-level model in Fig. 3a, we follow closely the approach applied to describe the photophysics of the silicon-vacancy colour centre in diamond³². First, we take the limiting values for $W \rightarrow 0$ and $W = 800\text{kW cm}^{-2} \gg W_0$ as an approximation for $W \rightarrow \infty$ and obtain $\tau_1^0 = 5.3\text{ ns}$, $\tau_2^0 = 150\text{ ns}$, $\tau_2^\infty = 14.5\text{ ns}$ and $a^\infty = 6.4$. Under the assumption $k_{21} + k_{23} \gg k_{31}^0, k_{31}^\infty$ we calculate

$$k_{31}^0 = \frac{1}{\tau_2^0}, \quad (4)$$

$$k_{31}^\infty = \frac{1/\tau_2^\infty - (1 + a^\infty)/\tau_2^0}{a^\infty + 1} + k_{31}^0, \quad (5)$$

$$k_{23} = \frac{1}{\tau_2^\infty} - k_{31}^\infty, \quad (6)$$

$$k_{21} = \frac{1}{\tau_1^0} - k_{23}. \quad (7)$$

The excitation rate of V_{Si} is proportional to the laser power density $k_{12} = \sigma W$, where the absorption cross-section σ can be estimated to a first approximation from the saturation behavior of Fig. 2d as $\sigma = (hv/TW_0)(k_{23}k_{31}^0 + k_{21}k_{31}^0)/(k_{23} + k_{31}^0)$. Here, we take for the transmission coefficient at the SiC surface $T = 0.81$. We then fit the experimental data in Fig. 3d using the following set of equations with W_S in Equation (3) as the only free parameter:

$$\tau_{1,2} = \frac{2}{A \pm \sqrt{A^2 - 4B}}, \quad (8)$$

$$A = k_{12} + k_{21} + k_{23} + k_{31}, \quad (9)$$

$$B = k_{12}(k_{23} + k_{31}) + k_{31}(k_{21} + k_{23}). \quad (10)$$

Finally, we fit all the data in Fig. 3c–e allowing to vary σ and a^∞ and using

$$a = \frac{1 - \tau_2 k_{31}}{k_{31} (\tau_2 - \tau_1)}. \quad (11)$$

From the best fits, shown by the solid lines in Fig. 3c–e, we obtain $W_S = 75\text{kW cm}^{-2}$ and $a^\infty = 7.5$. The obtained value for σ is presented in Table 1.

References

1. Waldherr, G. *et al.* Quantum error correction in a solid-state hybrid spin register. *Nature* **506**, 204–207 (2014).
2. Togan, E. *et al.* Quantum entanglement between an optical photon and a solid-state spin qubit. *Nature* **466**, 730–734 (2010).
3. De Greve, K. *et al.* Quantum-dot spin-photon entanglement via frequency downconversion to telecom wavelength. *Nature* **491**, 421–425 (2012).
4. Mamin, H. J. *et al.* Nanoscale nuclear magnetic resonance with a nitrogen-vacancy spin sensor. *Science* **339**, 557–560 (2013).
5. Staudacher, T. *et al.* Nuclear magnetic resonance spectroscopy on a (5-nanometer)³ sample volume. *Science* **339**, 561–563 (2013).
6. Atatüre, M., Dreiser, J., Badolato, A. & Imamoglu, A. Observation of Faraday rotation from a single confined spin. *Nat. Phys.* **3**, 101–106 (2007).
7. Balasubramanian, G. *et al.* Ultralong spin coherence time in isotopically engineered diamond. *Nat. Mater.* **8**, 383–387 (2009).
8. Siyushev, P. *et al.* Coherent properties of single rare-earth spin qubits. *Nat. Commun.* **5**, 3895 (2014).
9. Nothaff, M. *et al.* Electrically driven photon antibunching from a single molecule at room temperature. *Nat. Commun.* **3**, 628 (2012).
10. Koehl, W. F., Buckley, B. B., Heremans, F. J., Calusine, G. & Awschalom, D. D. Room temperature coherent control of defect spin qubits in silicon carbide. *Nature* **479**, 84–87 (2011).
11. Soltamov, V. A., Soltamova, A. A., Baranov, P. G. & Proskuryakov, I. I. Room temperature coherent spin alignment of silicon vacancies in 4H- and 6H-SiC. *Phys. Rev. Lett.* **108**, 226402 (2012).
12. Kraus, H. *et al.* Room-temperature quantum microwave emitters based on spin defects in silicon carbide. *Nat. Phys.* **10**, 157–162 (2014).
13. Baranov, P. G. *et al.* Silicon vacancy in SiC as a promising quantum system for single-defect and single-photon spectroscopy. *Phys. Rev. B* **83**, 125203 (2011).
14. Wagner, M. *et al.* Electronic structure of the neutral silicon vacancy in 4H and 6H SiC. *Phys. Rev. B* **62**, 16555–16560 (2000).

15. Carlos, W. E., Glaser, E. R. & Shanabrook, B. V. Optical and magnetic resonance signatures of deep levels in semi-insulating 4H SiC. *Physica B* **340–342**, 151–155 (2003).
16. Riedel, D. *et al.* Resonant addressing and manipulation of silicon vacancy qubits in silicon carbide. *Phys. Rev. Lett.* **109**, 226402 (2012).
17. Stucki, D. *et al.* High rate, long-distance quantum key distribution over 250 km of ultra low loss fibres. *New J. Phys.* **11**, 075003 (2009).
18. Vlasov, Y. A. & McNab, S. J. Losses in single-mode silicon-on-insulator strip waveguides and bends. *Opt. Express.* **12**, 1622–1631 (2004).
19. Kurtsiefer, C., Mayer, S., Zarda, P. & Weinfurter, H. Stable solid-state source of single photons. *Phys. Rev. Lett.* **85**, 290–293 (2000).
20. Castelletto, S. *et al.* A silicon carbide room-temperature single-photon source. *Nat. Mater.* **13**, 151–156 (2013).
21. Fuchs, F. *et al.* Silicon carbide light-emitting diode as a prospective room temperature source for single photons. *Sci. Rep.* **3**, 1637 (2013).
22. Yuan, Z. *et al.* Electrically driven single-photon source. *Science* **295**, 102–105 (2001).
23. Kraus, H. *et al.* Magnetic field and temperature sensing with atomic-scale spin defects in silicon carbide. *Sci. Rep.* **4**, 5303 (2014).
24. Bockstedte, M., Heid, M. & Pankratov, O. Signature of intrinsic defects in SiC: *ab initio* calculations of hyperfine tensors. *Phys. Rev. B* **67**, 193102 (2003).
25. Gali, A. Excitation spectrum of point defects in semiconductors studied by time-dependent density functional theory. *J. Mater. Res.* **27**, 897–909 (2012).
26. Mizuchi, N. *et al.* Continuous-wave and pulsed EPR study of the negatively charged silicon vacancy with $S = 3/2$ and C_{3v} symmetry in n-type 4H-SiC. *Phys. Rev. B* **66**, 235202 (2002).
27. Hain, T. C. *et al.* Excitation and recombination dynamics of vacancy-related spin centers in silicon carbide. *J. Appl. Phys.* **115**, 133508 (2014).
28. Sörman, E. *et al.* Silicon vacancy related defect in 4H and 6H SiC. *Phys. Rev. B* **61**, 2613–2620 (2000).
29. Heissenstein, H., Peppermüller, C. & Helbig, R. Characterization of phosphorus doped n-type 6H-silicon carbide epitaxial layers produced by nuclear transmutation doping. *J. Appl. Phys.* **83**, 7542 (1998).
30. Ionov, A. N. *et al.* Neutron transmutation doping of silicon 30Si monoisotope with phosphorus. *Techn. Phys. Lett.* **32**, 550–553 (2006).
31. Aharonovich, I., Castelletto, S., Simpson, D. A., Greentree, A. D. & Prawer, S. Photophysics of chromium-related diamond single-photon emitters. *Phys. Rev. A* **81**, 043813 (2010).
32. Neu, E. *et al.* Single photon emission from silicon-vacancy colour centres in chemical vapour deposition nano-diamonds on iridium. *New J. Phys.* **13**, 025012 (2011).
33. Yakovlev, D. R. *et al.* Charged exciton dynamics in ZnSe/ZnMgSSe QWs. *Phys. Status Solidi A* **178**, 501–505 (2000).
34. Bockstedte, M., Mattausch, A. & Pankratov, O. *Ab initio* study of the annealing of vacancies and interstitials in cubic SiC: vacancy-interstitial recombination and aggregation of carbon interstitials. *Phys. Rev. B* **69**, 235202 (2004).
35. Castelletto, S. *et al.* Room temperature quantum emission from cubic silicon carbide nanoparticles. *ACS Nano* **8**, 7938–7947 (2014).
36. Marseglia, L. *et al.* Nanofabricated solid immersion lenses registered to single emitters in diamond. *Appl. Phys. Lett.* **98**, 133107 (2011).
37. Calusine, G., Politi, A. & Awschalom, D. D. Silicon carbide photonic crystal cavities with integrated color centers. *Appl. Phys. Lett.* **105**, 011123 (2014).
38. Muzha, A. *et al.* Room-temperature near-infrared silicon carbide nanocrystalline emitters based on optically aligned spin defects. *Appl. Phys. Lett.* **105**, 243112 (2014).
39. Christle, D. J. *et al.* Isolated electron spins in silicon carbide with millisecond coherence times. *Nat. Mater.* **14**, 160–163 (2015).
40. Widmann, M. *et al.* Coherent control of single spins in silicon carbide at room temperature. *Nat. Mater.* **14**, 164–168 (2015).

Acknowledgements

This work has been supported by the German Research Foundation (DFG) under grant AS 310/4 and by the Bavarian State Ministry of Science, Research and the Arts within the Collaborative Research Network Solar Technologies Go Hybrid. We thank R. Bergmann and M. Villa for assistance with neutron irradiation and N. Wolf for help with annealing.

Author contributions

F.F., B.S. and D.S. conducted the experiments. F.F. and B.S. analyzed the experimental data. M.T. was responsible for neutron irradiation. J.P., V.D. and G.V.A. conceived the experiments. V.D. and G.V.A. wrote the manuscript with contribution from all authors.

Additional information

Supplementary Information accompanies this paper at <http://www.nature.com/naturecommunications>

Competing financial interests: The authors declare no competing financial interests.

Reprints and permission information is available online at <http://npg.nature.com/reprintsandpermissions/>

How to cite this article: Fuchs, F. *et al.* Engineering near-infrared single-photon emitters with optically active spins in ultrapure silicon carbide. *Nat. Commun.* **6**:7578 doi: 10.1038/ncomms8578 (2015).